The spatial origin of -5/3 spectra in grid-generated turbulence

S. Laizet, J. Nedić and J.C. Vassilicos[1]

Turbulence, Mixing and Flow Control Group,

Department of Aeronautics, Imperial College London

London, SW7 2AZ, United Kingdom.[a]

(Dated: 10 June 2015)

A combined wind tunnel and computational study of grid-generated turbulence along the centreline shows that the close to $-5/3$ power law signature of energy spectra in the frequency domain originates relatively close to the grid where the velocity derivative statistics become quite suddenly isotropic but also where the turbulent fluctuating velocities are very intermittent and non-Gaussian. As the inlet flow velocity increases, these power laws are increasingly well defined and increasingly close to $-5/3$ over an increasing range of frequencies. However, this range continuously decreases with streamwise distance from the grid even though the local Reynolds number first increases and then decreases along the same streamwise extent. The intermittency at the point of origin of the close to $-5/3$ power spectra consists of alternations between intense vortex tube clusters with shallow broad-band spectra and quiescent regions where the velocity fluctuations are smooth with steep energy spectra.

---

[a]Electronic mail: s.laizet@imperial.ac.uk, j.c.vassilicos@imperial.ac.uk

I. INTRODUCTION

Ten years after Kolmogorov[1,2]'s prediction of the turbulent energy spectrum's $-5/3$ wavenumber scaling,[3] launched a research activity concerned with the flow morphology underlying this $-5/3$ spectrum. He noted that the spectral signature of a vortex tube has a k^{-1} wavenumber range (where k is the wavenumber) whereas the spectral signature of a vortex sheet has a k^{-2} range. Kolmogorov's $-5/3$ lies in between and therefore[3] speculated that the inner morphology of a turbulent fluctuation field might consist of random collections of both vortex tubes and vortex sheets. A few years later,[4] showed that the down-scale nature of Kolmogorov's turbulent cascade means that vortex sheets should in some sense dominate.

Other works in this direction followed, notably by[5],[6] and[7]. In particular,[6] proposed a model of the small-scale turbulence structure which consists of contorted and curved vortex tubes. Fourteen years later,[8] took a similar approach, also based on tubes, but with a spiral vortex sheet rolled up around the tube.[8]'s spiral vortex sheet combines the tube and sheet morphologies and is consistent with the tendency of sheet-like structures to roll up. It is an approximate solution of the Navier-Stokes equation and has, when integrated over time, a power-law energy spectrum of the form $\epsilon^{2/3}k^{-5/3}$ where ϵ is the kinetic energy dissipation rate per unit mass.[8]'s suggestion is that the small-scale turbulence consists of randomly distributed local spiral vortex sheet solutions of the Navier-Stokes equation and that these local spiral vortex sheet structures are responsible for the $\epsilon^{2/3}k^{-5/3}$ spectrum of the turbulence. [9] showed how the $k^{-5/3}$ wavenumber dependence of the energy spectrum of this vortex results from combined differential rotation and strain averaged over time.

Turbulent energy spectra with more or less approximate $-5/3$ power-law ranges have indeed been found in many high Reynolds number fully developed turbulent flows including turbulent wakes, jets, channels and boundary layers (see[10]). In turbulence generated by passive grids, such spectra are not present far downstream where the Reynolds number has dropped to values that are not high enough, but they are present (at least approximately) in the nearer field of such flows. This has historically been the turbulent flow of choice for testing Kolmogorov's theory because of the increased statistical homogeneity that the interactions between the different wakes emanating from the different bars on the grid can be expected to cause.

Grid-generated turbulence is a canonical flow of both fundamental and applied (turbulent

mixing) importance and it is therefore worth concentrating special attention to it. In grid-generated turbulence, along a streamwise centreline axis crossing midway between bars on the grid, the turbulence intensity increases first till it reaches a peak at a distance x_{peak} from the turbulence generator and then continuously decays further downstream (see[11],[12],[13] and[14]). In a sizeable streamwise portion of the decay region which corresponds to at least a few turnover times from x_{peak}, the scaling of the turbulence dissipation rate has been found to be different from the well-known Kolmogorov scaling, yet the dependence of the energy spectrum $E(k)$ on wavenumber k is $k^{-5/3}$ in a significant intermediate range of wavenumbers (see[15] and references therein). Further downstream where the scaling of the dissipation rate suddenly becomes classical even though the local Reynolds number has dropped to relatively low values ([16],[17],[18]) there is no clear Kolmogorov signature whatsoever in the turbulent energy spectrum ([18]).

Even though $E(k) \sim k^{-5/3}$ is not accountable to the Richardson-Kolmogorov equilibrium cascade in the region of grid-generated turbulence where it has been observed (see[15]), it must nevertheless be related to a near-singular flow structure ([19],[20]) perhaps (though not necessarily) of the localised kind discussed by[3],[5],[6],[7] and[8]. In this paper we attempt to describe some of the properties of the flow and its inner morphology at the closest centreline streamwise point to the grid where the turbulent energy spectrum acquires a clear $k^{-5/3}$. We also describe how the $-5/3$ range varies with Reynolds number and streamwise distance from the grid.

Recent Direct Numerical Simulations (DNS) by[21] have suggested that the $k^{-5/3}$ wavenumber scaling of the turbulent energy spectrum has, in fact, its spatial origin midway in the production region $0 < x < x_{peak}$ where x is the streamwise distance from the grid. However, the spatial resolutions of their DNS has been shown by[22] to be insufficient in some respects and the water channel experiments of[23] did not find evidence of such a scaling at that point. These water channel experiments suffered from significant uncontrolled free-stream turbulence at the inlet which could have affected the results of[23] in the production region. It is therefore important to take wind tunnel measurements in the production region under cleaner conditions with very low background turbulence and run DNS with the high resolution recommended by[22]. In this paper we report results from such measurements and such DNS.

We follow[21] and[23] in that we do not use classical regular grids because the production

region of such grids is extremely short, in fact confined to the immediate neighbourhood of the grids, and because the turbulence intensity in the production region of such grids is extremely high (up to and above 20%). To facilitate the use of hot wire measurements and limit the demands on our DNS resolution in the production region we use four different passive grids of the types used by[21],[23] and[24],[25] all designed such that the production region upstream of the decay region is quite long and with moderate turbulence intensities.

We therefore conduct wind tunnel experiments of turbulence generated by two different fractal grids (FSG8 and FSG17 in figure 1 and table 1) and two different single mesh grids (RG230 and SSG in figure 1 and table 1). We also carry out Direct Numerical Simulations (DNS) of turbulence generated by the FSG8 and SSG grids. We concentrate our attention on the streamwise centreline axis and record data starting from very close to the grids at distances well below x_{peak} to distances larger than x_{peak}. This way we are able to identify the closest point to the grids where $-5/3$ spectra appear in the frequency domain and document the way they develop as functions of streamwise coordinate x and the way they depend on Reynolds number. We also describe how the $-5/3$ range varies with streamwise distance from the grid.

Our combined wind tunnel and DNS results show quite clearly that the $-5/3$ spectra originate inside the production region $x < x_{peak}$ around a position x_{53} rather close to the grid where the velocity derivative statistics become quite suddenly isotropic but also where the turbulent fluctuating velocities are very intermittent and non-Gaussian. These $-5/3$ power laws are increasingly well defined over an increasing range of frequencies for increasing inlet flow velocities U_∞. But this range also continuously decreases as x increases beyond x_{53}.

Furthermore, our DNS results show that the intermittency at x_{53} consists of alternations between vortex tube clusters with shallow broad-band spectra and quiescent regions where the velocity fluctuations are smooth with steep energy spectra. The -5/3 frequency scaling of the energy spectrum seems to originate in such an intermittent flow region.

In sections II and III we present our experimental and computational set-ups and in section IV our results. We conclude in section V where we also formulate a few questions for the future, in particular the implications of our results on wavenumber spectra. This is the topic of Appendix A where this paper's DNS are used to investigate the Taylor frozen turbulence hypothesis.
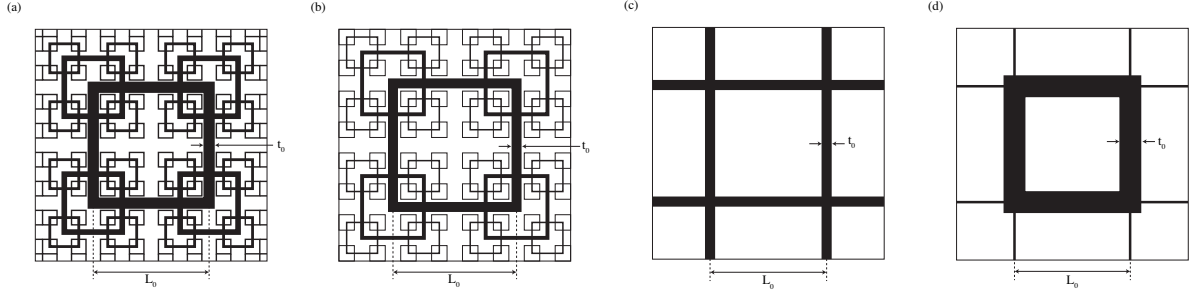
4

FIG. 1. Turbulence generating grids. From left to right, FSG8, FSG17, RG230 and SSG. The length L_0 and the thickness t_0 are defined in the pictures. The streamwise thickness of all the grids is $6mm$ except for the FSG17 grid for which it is $5mm$. All four grids were tested in the wind tunnel but Direct Numerical Simulations were carried out only for FSG8 and SSG. The thin supporting bars seen in the SSG figure were not included in the simulations. The figures are to scale and represent the scaled-down size of the test section. There are $N = 4$ fractal iterations in FSG8 and FSG17. The side length of the repeated squares is divided by 2 at each iteration. See table 1 for more details.

II. EXPERIMENTAL SET-UP

Experimental runs were conducted for each one of our grids (see figure 1 and Table 1) with the grid placed at the test section entry of our 0.4572m $\times$ 0.4572m (18" $\times$ 18") blow down wind tunnel. The test section is 3.5m long and the background turbulence level at the wind tunnel speeds we applied is about 0.1%. A mesh is installed at the entrance of the diffuser to maintain a slight over-pressure in the test section. The inlet velocity U_∞ is controlled using the static pressure difference across the 8:1 contraction, the temperature taken near the diffuser and the atmospheric pressure from a pressure gauge, all of which were measured using a Furness Controls micromanometer FCO510. The turbulence generating grids are shown in figure 1 and the parameters defining them are given in table 1. Note that all four grids have one large square in common which is of approximate similar dimensions in all cases except for SSG where the thickness t_0 is about double. This allows the SSG to return comparable local Reynolds numbers as the FSG8.

Measurements of the velocity signal were taken along the centreline using a DANTEC 55P01 hot-wire ($5\mu m$ in diameter with a sensing length of 1.25mm), driven by a DANTEC Streamline anemometer with an in-built signal conditioner running in constant-temperature

mode. The spatial intervals of our measurements were such that there was increased resolution closer to the grid specifically in the production region $x < x_{peak}$ compared to the decay region $x > x_{peak}$. For example, the spatial interval for the FSG8 grid was $0.02x_*$ for $x \leq 0.3x_*$, $0.05x_*$ for $0.35x_* \leq x \leq 0.5x_*$ and $0.1x_*$ for $0.6x_* \leq x \leq x_*$ (see table 1 and its caption for a definition of x_* and for values of x_{peak}/x_*). Data were sampled using a 16-bit National Instruments NI-6229(USB) data acquisition card for $300s$ at a sampling frequency of 100kHz, with the analogue low-pass filter on the Streamline set to 30kHz. Each data set was then digitally filtered, using a fourth-order Butterworth filter to eliminate high frequency noise, at a frequency higher than 1.5 times the Kolmogorov frequency.

III.   NUMERICAL SET-UP

DNS were conducted only for the FSG8 and SSG grids (see figure 1 and table 1 where t_0 and L_0 are also defined). The streamwise thickness for both grids is $0.25t_0$. The computational domain in the streamwise x and the two lateral y and z directions is $L_x \times L_y \times L_z = 16L_0 \times 2L_0 \times 2L_0$ for the FSG7 and $L_x \times L_y \times L_z = 8L_0 \times 2L_0 \times 2L_0$ for the SSG. It is discretized on a Cartesian mesh using $n_y \times n_z = 720 \times 720$ mesh nodes in lateral planes and $n_x = 5761$ and $= 2881$ in the streamwise direction for the FSG8 and SSG respectively. The coordinate system's origin is placed at the centre of the grid which is located at a distance of $1.25L_0$ from the inlet of the computational domain in order to avoid spurious interactions between the grid and the inlet condition.

We assume a fluid of uniform density and kinematic viscosity ν. Inflow/outflow boundary conditions are used in the streamwise direction and periodic boundary conditions are used in the two lateral directions. The inflow and initial conditions for the velocity field are $\mathbf{u} \equiv (u, v, w) = (U_\infty, 0, 0)$ where U_∞ is a constant streamwise velocity (u is the streamwise velocity component and (v, w) are the two lateral velocity components corresponding to (y, z)). The outflow condition is a standard 1D convection equation.

We solve the incompressible Navier-Stokes equations

$$\frac{\partial \mathbf{u}}{\partial t} + \frac{1}{2} \left(\nabla \cdot (\mathbf{u} \otimes \mathbf{u}) + (\mathbf{u} \cdot \nabla) \mathbf{u} \right) = -\frac{1}{\rho} \nabla p + \nu \Delta \mathbf{u} + \mathbf{f} \tag{1}$$

$$\nabla \cdot \mathbf{u} = 0 \tag{2}$$

on a Cartesian mesh with our numerical code **Incompact3d** which is based on sixth-order

6

Grid	FSG8	FSG17	RG230	SSG
t_0 (mm)	22.23	19.2	20.0	43.18
L_0 (mm)	228.6	237.7	230.0	228.6
t_r	8	17	1	1
σ	0.42	0.25	0.17	0.19/0.21
$U_\infty (m/s)$	1.176/2.5/5/10	5/10	2.5/5/10	1.176/2.5/5/10
First $-5/3$ (x_*)	0.2/0.2/0.2/0.2	0.165/0.165	0.3/0.3/0.3	0.3/0.3/0.3/0.3
Peak u' (x_*)	0.325	0.4136	0.6	0.5
First Gaussian (x_*)	0.35	0.5147	0.8	0.7
$Re_\lambda(5/3)$	80/140/214/394	72/125	50/74/118	100/111/206/416

TABLE I. L_0 and t_0 are defined in figure 1 and the wake-interaction length-scale x_* equals L_0^2/t_0 (see[26] where the wake-interaction length-scale was introduced). Our fractal grids have $N = 4$ self-similar iterations and $t_r \equiv t_0/t_{N-1}$ where t_{N-1} is the thickness of the smallest bars. The ratio between consecutive bar thicknesses is $t_r^{1/(N-1)}$. The thickness ratio t_r (trivially equal to 1 for RG230 and SSG) is given in the 3rd line of the table and the blockage ratio σ in the 4th. For SSG, σ is 0.19 in the direct numerical simulation but 0.21 in the wind tunnel. The inlet flow velocities U_∞ used with each grid are given in the 5th line. All cases correspond to wind tunnel measurements except for the two $U_\infty = 1.176m/s$ cases which are Direct Numerical Simulations. The 6th and last lines give the corresponding approximate values of x_{53} (where the first power-law spectrum with exponent close to $-5/3$ appears) in multiples of x_* and the corresponding values of Re_λ at this point. The streamwise distance x_{peak} from the grid along the centreline where the rms of the streamwise turbulent velocity peaks is given in the 7th line and the distance from the grid beyond which the turbulence is approximately Gaussian is given in the 8th line, both in multiples of x_*. (Values corresponding to the DNS in blue.)

compact schemes for spatial discretization and a third order Adams-Bashforth scheme for time advancement. To treat the incompressibility condition, a fractional step method requires solving a Poisson equation. This equation is fully solved in spectral space, via the use of relevant 3D Fast Fourier Transforms. The pressure mesh is staggered from the velocity mesh by half a mesh, to avoid spurious pressure oscillations. With the help of the concept

of modified wave number ([27]), the divergence-free condition is ensured up to machine accuracy. The modelling of the grids is performed by an Immersed Boundary Method, based on a direct forcing approach that ensures zero-velocity boundary condition at the grid walls. This approach mimics the effects of a solid surface on the fluid with an extra force $\mathbf{f}$ in the Navier-Stokes equations and takes advantage of our particular Cartesian mesh which conforms with the geometry of the turbulence-generating grid. Full details about the code, its validations and its application to grid-generated turbulence can be found in[28,29].

The size of the present simulations are such that we have no alternative but to use the parallel version of this code ([30]). Based on a highly scalable 2D decomposition library and a distributed FFT interface, it is possible to use the code on thousands of computational cores (more details about this efficient parallel strategy can be found in[30]).

Data are collected after the turbulence downstream of the grid has been fully developed. The data collection is over a period of $500,000$ time steps with a time step of $0.000139 L_0/U_\infty$ which is the same as the time step of the simulation. The data is therefore collected over a duration corresponding to $20s$ in the wind tunnel experiment. The time step is small enough for the CFL to be lower than 0.75 and for the smallest time scales η/U_∞ of our flows to be resolved. The spatial resolution has been investigated in detail in terms of the Kolmogorov microscale η (the smallest length-scale of the turbulence) in[22] where successful quantitative comparisons between the present DNS and wind tunnel measurements are also reported. Here the spatial resolution $\Delta x = \Delta y = \Delta z$ lies between 0.5η and 2η throughout the domain.

IV.   RESULTS

We start our investigations with examples in figure 2 of streamwise mean flow velocity maps obtained with our code upstream of but relatively close to the FSG8 grid. It is clear that the flow is non-homogeneous close to the grid in the region where the turbulence is buildiong up (see figure 3). One can also see that the imprint of the largest square of the fractal grid is noticeable in the mean flow gradients up to above $x = 0.4x_*$ (see Table 1).

An example of how the local Reynolds number Re_λ (based on the rms streamwise fluctuating velocity and the Taylor microscale shown in figure 3b) evolves along the centreline is given in figure 3a. One can observe a clear peak value of Re_λ demarcating the production
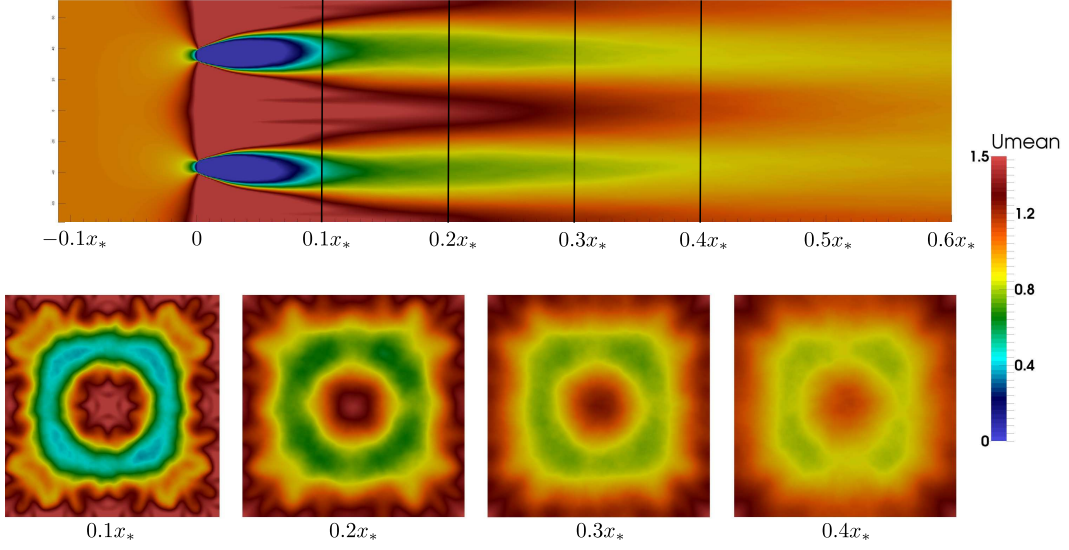
FIG. 2. Streamwise mean flow velocity maps for our FSG8 simulation (see table 1). The top map corresponds to the $y = 0$ centre-plane. The four bottom maps correspond to lateral (y, z) planes at, from left to right, $x = 0.1x_*$, $x = 0.2x_*$, $x = 0.3x_*$ and $x = 0.4x_*$ (see definition of x_* and comparisons with other meaningful lengths in table 1).
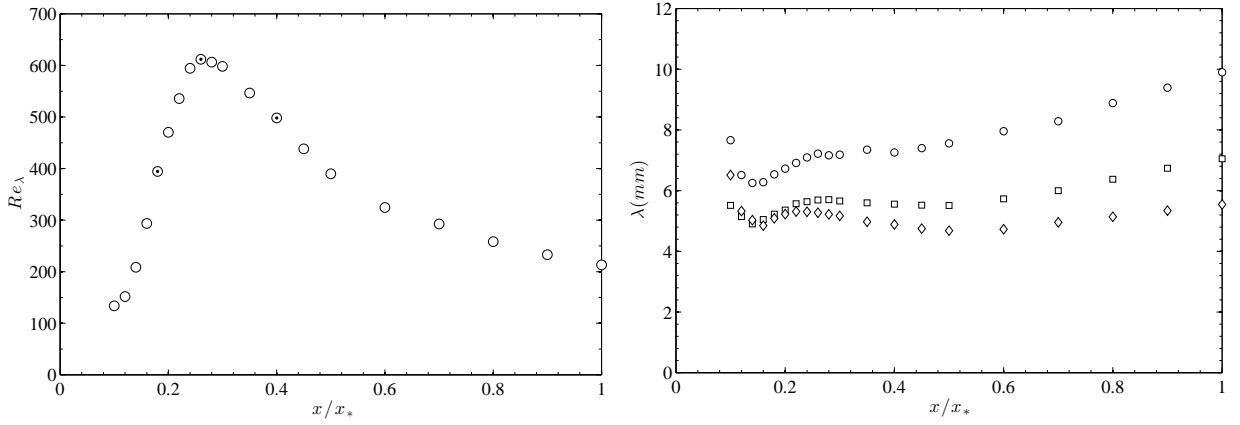

FIG. 3. Wind tunnel measurements with the FSG8 grid on the centreline. (Left) Streamwise evolution of Re_λ along the centreline at $U_\infty = 10m/s$. The black circles correspond to locations $x = 0.18x_*$, $x = 0.26x_*$ and $x = 0.4x_*$ which are analysed in more detail in figures 4 and 6. (Right) Streamwise evolution of the Taylor microscale along the centreline at $U_\infty = 2.5$, 5 and $10m/s$ ($\Diamond = 10m/s$, $\Box = 5m/s$, $\bigcirc = 2.5m/s$).
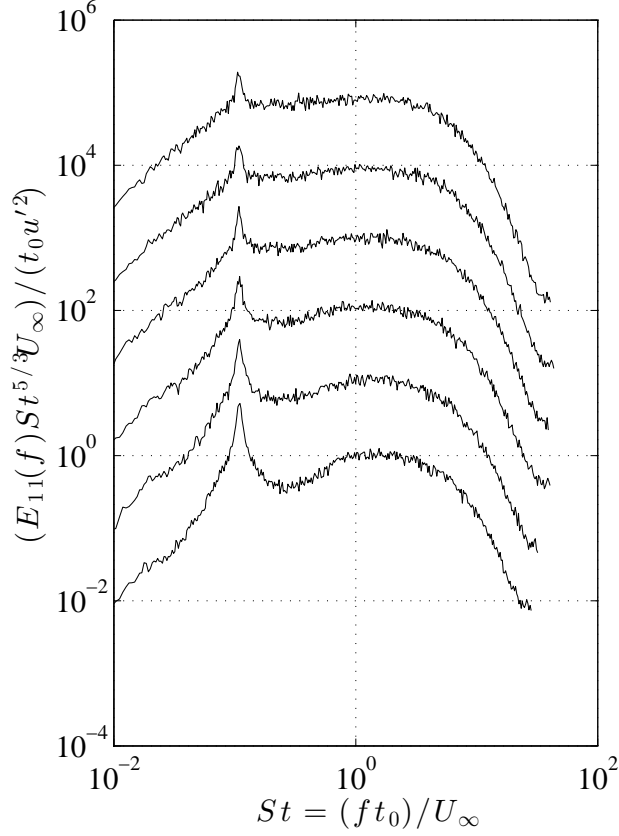
9

FIG. 4. Compensated energy spectra $E_{11}(f)St^{5/3}U_\infty/(t_0 u'^2)$ (where u' is the rms streamwise fluctuating velocity) versus the non-dimensional frequency St where $St = ft_0/U_\infty$. The spectra have been shifted along the vertical axis for clarity of presentation. From bottom to top the spectra correspond to $x/x_* = 0.1, 0.12, 0.14, 0.16, 0.18, 0.2$. FSG8 grid, $U_\infty = 10m/s$ and $x_{53}/x_* = 0.2$.

region upstream and the decay region downstream of the location of this peak. As expected, when the inlet velocity is increased the Taylor micro-scale is reduced. The turbulence intensity behaves in a very similar way with the local Reynolds number Re_λ and reaches a peak (at x_{peak}) which is under 15% for the FSG8 and SSG grids and under 8% for the other two grids. The measurements were taken along the centreline and therefore never behind an obstructing bar (see figure 1) so that there were no recirculating flow problems.

A thorough examination of streamwise fluctuating velocity component energy spectra $E_{11}(f)$ at many x-locations along the centreline revealed that these frequency spectra adopt, from a location x_{53} onwards (i.e. $x \geq x_{53}$), a well-defined power-law shape close to $f^{-5/3}$ over a significant range of frequencies f (we record x_{53} in table 1 for all our grids). An example of the way in which the spectra progressively shape up as x grows towards x_{53} is given in figure
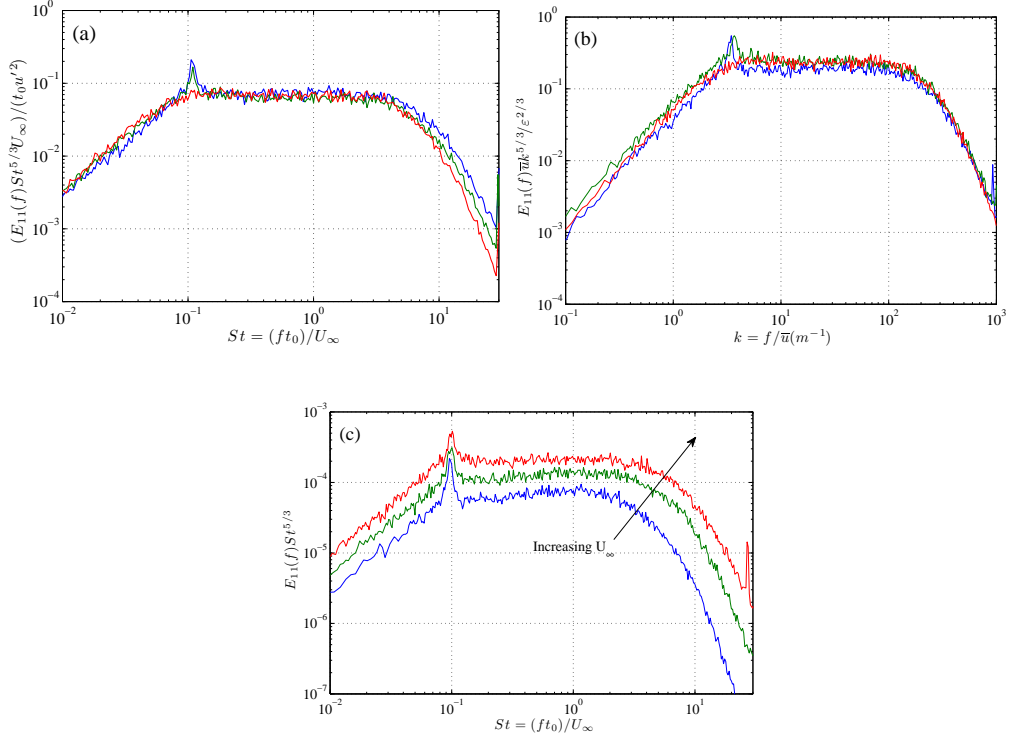
10

FIG. 5. Wind tunnel measurements with the FSG8 grid. (a) Log-log plot of compensated energy spectra $E_{11}(f)St^{5/3}U_\infty/(t_0u'^2)$ (where u' is the rms streamwise fluctuating velocity) versus the non-dimensional frequency St where $St = ft_0/U_\infty$. $U_\infty = 10m/s$. The three curves correspond to the three centreline positions x marked with black circles in figure 2. The curve with the most intense peak at St close to 10^{-1} and with the most energy at the highest frequencies is for $x = 0.18x_*$ (in blue). The curve without a peak at St close to 10^{-1} and with the least energy at the highest frequencies is for $x = 0.4x_*$ (in red). The other curve is for $x = 0.26x_*$ (in green). (b) Same as (a) but the log-log plot is now of compensated energy spectra $\overline{u}E_{11}(f)\epsilon^{-2/3}(f/\overline{u})^{5/3}$ versus $k = f/\overline{u}$ where $\overline{u}(x)$ is the streamwise mean flow velocity at x. (c) Log-log plot of $E_{11}(f)St^{5/3}$ versus St for at $x = 0.2x_*$ for $U_\infty = 2.5m/s$ (blue), $5m/s$ (green) and $10m/s$ (red).

4. Energy seems to progressively fill the gap between the vortex shedding frequency and the frequencies were $St > 1$ leading, at $x = x_{53}$, to a well-defined $f^{-5/3}$ power-law spectrum. The location x_{53} differs for fractal and non-fractal grids: it is more or less between $0.16x_*$ and $0.2x_*$ for the fractal grids and around $0.3x_*$ for the RG230 and SSG grids (see table 1). Interestingly x_{53} is about the same for all the values of U_∞ that we tried, between $2.5m/s$ and $10m/s$ in the wind tunnel and $U_\infty = 1.176m/s$ in our simulations (see table 1).

11

An example of $E_{11}(f)$ at $x \approx x_{53}$ is given in figure 4 where we also plot $E_{11}(f)$ at two values of x larger than x_{53}, one at $x = 0.26x_*$ where Re_λ reaches its maximum along the centreline and one at $x = 0.4x_*$ which is in the decay region but where Re_λ is still larger than at $x \approx x_{53}$ (see figure 3). The position x_{53} where a spectrum close to $f^{-5/3}$ first appears is, for all grid cases, in the production region, i.e. where $x < x_{peak}$. As x increases beyond x_{53} the range over which the $-5/3$ spectrum is present diminishes (see figure 5a) even if Re_λ does not diminish (figure 3). In fact, depending on grid and inlet velocity U_∞, the value of Re_λ at position x_{53} can take a variety of values over a wide range (from 80 to about 400 for the cases recorded in table 1). The local Reynolds number Re_λ therefore seems to play a limited role here. It is the inlet Reynolds number based on U_∞ which seems to determine the extent of the $f^{-5/3}$ spectrum. An example of this phenomenon is clear in figure 5c where, at a fixed value of x close to x_{53}, the part of $E_{11}(f)$ which is close to $f^{-5/3}$ gets closer to such a power law over a wider range of frequencies as U_∞ increases.

Turning now to the magnitude, rather than the frequency extent, of the spectrum, figure 5a,b shows that it is not captured by Kolmogorov scaling and the Taylor frozen turbulence hypothesis which is required to translate this scaling into the frequency domain. Indeed, the power-law part of the spectrum scales as $U_\infty E_{11}(f) \sim \frac{u'^2}{t_0^{2/3}}(f/U_\infty)^{-5/3}$ (see figure 5a) and not $\overline{u} E_{11}(f) \sim \epsilon^{2/3}(f/\overline{u})^{-5/3}$ (see figure 5b) which does not collapse the data as well. In Appendix A we show that the Taylor hypothesis can anyway not be justifiably used at normalised frequencies St smaller than about 1 or 2 at the flow locations considered here.

The appearance around x_{53} of spectra which include a power law form close to $f^{-5/3}$ is accompanied by a rather sudden collapse of all small-scale isotropy indicators K_n to values close to the isotropic value 1 (see figure 6). The definition of the ratios K_n (originally introduced by[31]) are given in the caption of figure 6. They are very commonly used as local isotropy diagnostics (e.g. see[32]). It is striking how the values of K_n cluster around 1 at $x \geq 0.3x_*$ in the SSG case (figure 6, left) but at $x \geq 0.18x_*$ in the FSG8 case (figure 6, right), particularly because power law spectra with exponents close to $-5/3$ appear at $x \approx 0.3x_*$ in the SSG case but at $x \approx 0.2x_*$ in the FSG8 case. The appearance of such spectra seems to be correlated with the appearance of small scale isotropy close to the grid, i.e. at a distance between 1.5 and 2 times L_0 from the grid.

Even though the small scale turbulence appears locally isotropic at x_{53} and further downstream, the fluctuating velocities are not Gaussian in the production region $x < x_{peak}$ (x_{53} is
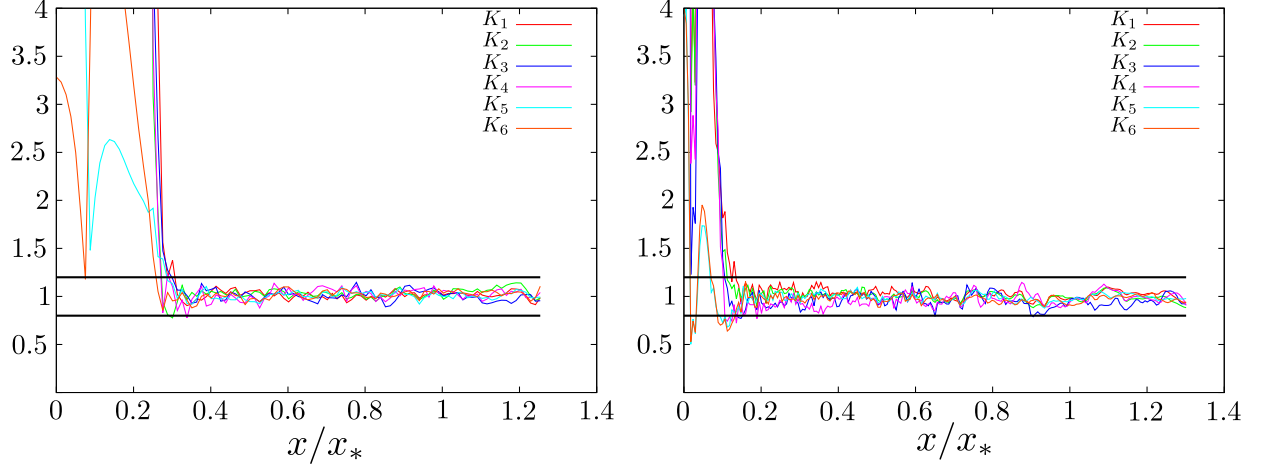
FIG. 6. Local isotropy diagnostics obtained from our high-resolution simulations for the FSG8 (left) and SSG (right) grids. $K_1 = \frac{2\langle(\partial u/\partial x)^2\rangle}{\langle(\partial v/\partial x)^2\rangle}$, $K_2 = \frac{2\langle(\partial u/\partial x)^2\rangle}{\langle(\partial w/\partial x)^2\rangle}$, $K_3 = \frac{2\langle(\partial u/\partial x)^2\rangle}{\langle(\partial u/\partial y)^2\rangle}$, $K_4 = \frac{2\langle(\partial u/\partial x)^2\rangle}{\langle(\partial u/\partial z)^2\rangle}$, $K_5 = \frac{\langle(\partial u/\partial x)^2\rangle}{\langle(\partial v/\partial y)^2\rangle}$, $K_6 = \frac{\langle(\partial u/\partial x)^2\rangle}{\langle(\partial w/\partial z)^2\rangle}$.

smaller than x_{peak} by a factor between 1.5 and 2, see table 1) and their probability density functions (PDF) start approximating a Gaussian only at a distance x slightly larger than x_{peak} (see table 1). In figure 7 we plot examples of fluctuating streamwise velocity signals and their PDFs at the three positions marked with black circles in figure 3. In terms of K_n, there is local isotropy at all three locations, yet the turbulence is widely non-Gaussian at $x = 0.18x_*$ (which is very close or even corresponds to x_{53} for this particular grid), significantly non-Gaussian at $x = 0.26x_*$ where Re_λ peaks (see figure 3) and starts approximating a Gaussian at $x = 0.4x_*$ which is larger than x_{peak} for this grid (FSG8). Plots of the skewness and the flatness of the fluctuating streamwise velocity for the FSG8 grid suggest that the turbulence is Gaussian upstream of $x/x_* = 0.4$ as shown in figure 8. Indeed at $x \geq 0.4x_*$, the skewness is zero and the flatness is equal to 3, as expected when the PDF of the streamwise turbulence intensity is Gaussian. It is interesting that the close to $-5/3$ power-law form of the spectrum originates at a location relatively near the turbulence-generating grid where the turbulence is so non-Gaussian. What does this non-Gaussianity correspond to?

To answer this question we use our DNS because it provides access to 3D velocity and vorticity fields. In figure 9 we show a time-trace of the derivative with respect to the streamwise coordinate of the fluctuating streamwise velocity component and a time-trace of the streamwise fluctuating velocity component, both at $x = 0.3x_*$ (i.e. $x \approx x_{53}$) on the
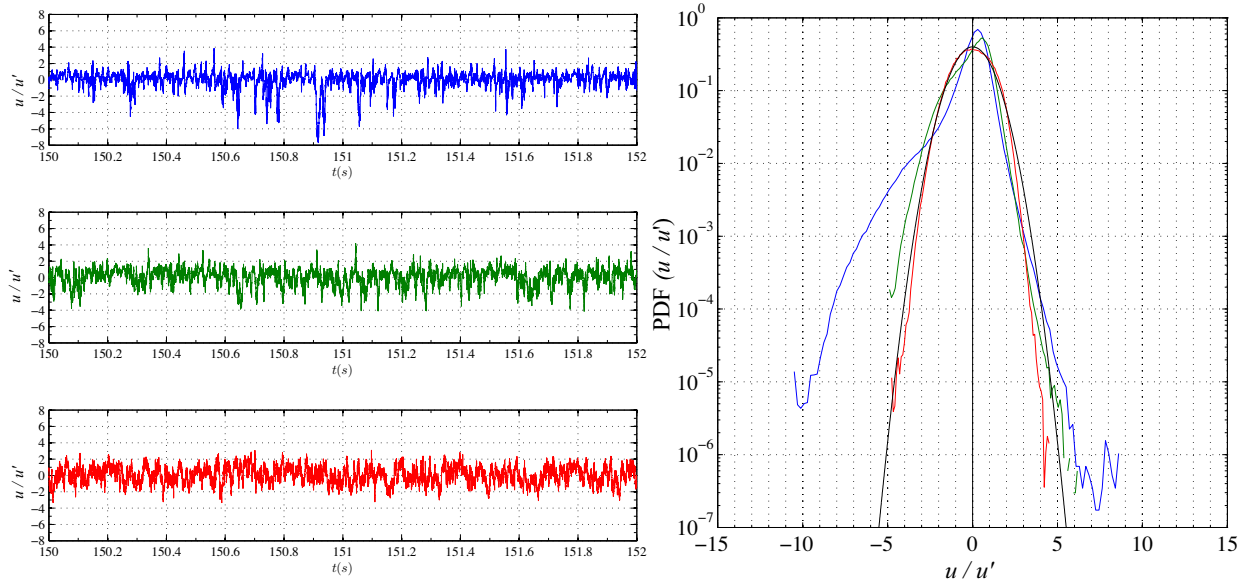
13

FIG. 7. Wind tunnel measurements with the FSG8 grid at $U_\infty = 10m/s$. (Left) Time traces of fluctuating streamwise velocities ($u = U - \overline{u}$) corresponding to, from top to bottom, the three centreline positions x marked with black circles in figure 3. (Right) Log-linear plot of the PDFs of these streamwise fluctuating velocity components with a Gaussian curve for reference. The PDF closest to the Gaussian is for $x = 0.4x_*$ and corresponds to the bottom left trace on the left (in red). The PDF with the widest discrepancy from the Gaussian is for $x = 0.18x_*$ and corresponds to the top left trace on the left (in blue).The PDF in between is for $x = 0.26x_*$ and corresponds to the middle trace on the left (in green).

centreline for the SSG. The alternation between quiescent regions such as Q1 and Q2 and regions with intense and irregular local fluctuations such as I1 and I2 is clear. In fact the top plot in figure 9 distinguishes between intense and quiescent events particularly clearly. The actual extent of each event does not matter much, as the high frequencies are present regardless of the choice of this extent, and changing it will mainly change the low frequency part of the spectra at the bottom of figure 9. These are the energy spectra in the frequency domain of Q1 and I1 on the left and of Q2 and I2 on the right. The extent of these events is such that the range of frequencies shown in their energy spectra is comparable. We find that the quiescent events have a very steep spectra fluctuating around f^{-6} and no energy content for normalised frequencies $St \equiv ft_0/U_\infty$ larger than about 7 or 8. A slope steeper than -4 implies that there are no singularities in the fluctuating velocity signal or its first
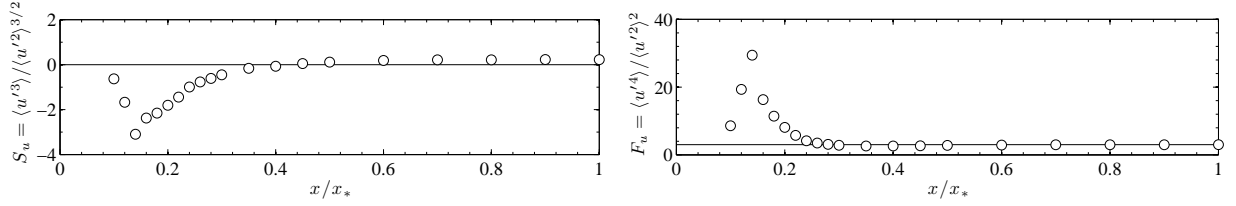
14

FIG. 8. Wind tunnel measurements with the FSG8 grid at $U_\infty = 10m/s$. Skewness (left) and flatness (right) of the fluctuating streamwise velocity component as functions of normalised streamwise distance x/x_* from the grid.

derivative, in agreement with the fact that the signals at the quiescent regions are quite smooth. The intense events have much more fluctuating energy than the quiescent regions and much shallower spectra over a wider range of frequencies, in fact shallower than f^{-2}. The spectrum of the entire signal is included in the plots for comparison and it exhibits a sufficiently well-defined $f^{-5/3}$ spectrum from $St \approx 0.3$ to $St \approx 6$. The spectra of the intense events are not all the same but they do seem to oscillate around a power law close to $f^{-5/3}$ between $St \approx 1$ and $St \approx 6$, in particular for I2. It is clear that the resulting $f^{-5/3}$ spectrum of the entire signal would be impossible without them.

To see what these intense events correspond to we plot in figure 9 three-dimensional (3D) visualisations of the enstrophy field in a region of the flow centred around $x = 0.3x_*$ on the centreline. This is the location where the data for figure 9 have been recorded in time. Figure 10 shows the enstrophy field at different times within the time frame of intense event I2 (see figure 9). It can be seen that this intense event corresponds to the passage of a cluster of entangled intense vortex tubes. Similar 3D enstrophy visualisations corresponding corresponding to Q1 and Q2 do not show anything unless the enstrophy iso-contour level is taken to be about two orders of magnitude smaller than in figure 10. The $-5/3$ frequency spectrum and the local isotropy (figure 6) which first appear at $x = x_{53}$, relatively close to the grid, and which survive downstream (albeit over a diminishing range of frequencies for the spectrum) have their origin in such vortex tube clusters. These vortex tube clusters originate from the wakes of the bars making the grid. However, we checked that energy spectra recorded at positions inside these wakes, i.e. in the lee of the blocking bars, do not have as well-defined -5/3 spectra as on the centreline. We also checked that the turbulent fluctuating velocities in these wakes are also much closer to Gaussian than they are on the

15

centreline at comparable values of x.

One important side implication of the work by[8] which we referred to in the introduction is that the $k^{-5/3}$ spectrum is not specific to fully developed small-scale turbulence but can also be found in other flows. Power-law energy spectra have indeed been found in the very near wake of cylinders (within one to a few cylinder diameters from the cylinder, see[33,34]), but the power-law exponent is not quite $-5/3$ though not too far from it either. Directly inspired by[8]'s work,[35,36] created a spiral vortex flow in a laminar environment in the laboratory. Their flow was cyclical in time, alternating between a very well defined spiral vortex sheet and a vortex burst, and the resulting time-averaged energy spectrum had a relatively clear $-5/3$ power-law shape over a significant range. It may be that something similar is happening with the present vortex tube clusters which are found at a position where the turbulence is not fully developed, midway between the turbulence-generating grid and the position x_{peak} of the turbulence intensity peak. However the -5/3 power-law scaling of energy spectra appears to be a wider phenomenon as such spectra have also been found in solutions of conservative and time-reversilbe truncated 3D incompressible Euler equations (see[37]). This aspect of the problem requires a full investigation of its own and will be the object of a future publication.

V.   CONCLUSION AND DISCUSSION

On the centreline of grid-generated turbulence with grids where the centreline runs midway between solid bars, the $f^{-5/3}$ energy spectrum originates at a point x_{53} in the production region, about midway between the grid and the position x_{peak} of the turbulence intensity peak. The $f^{-5/3}$ spectrum is increasingly well-defined over an increasing range of frequencies for higher inlet velocities U_∞ and remains present, albeit over a continuously diminishing range of frequencies, with increasing downstream distance from x_{53}. The turbulence becomes suddenly locally isotropic at x_{53}, i.e. the velocity derivative indicators K_n are different from 1 for $x < x_{53}$ but equal to 1 for $x \geq x_{53}$. The combined appearance of local isotropy and of a near-5/3 power-law spectrum at x_{53} happens irrespective of the local value of Re_λ. This should not be confused with a Kolmogorov spectrum because figure 5a shows clearly that the power-law part of the spectrum scales as $U_\infty E_{11}(f) \sim \frac{u'^2}{t_0^{2/3}}(f/U_\infty)^{-5/3}$ and not $\overline{u}E_{11}(f) \sim \epsilon^{2/3}(f/\overline{u})^{-5/3}$ which we also tried (see figure 5b) and which does not collapse the
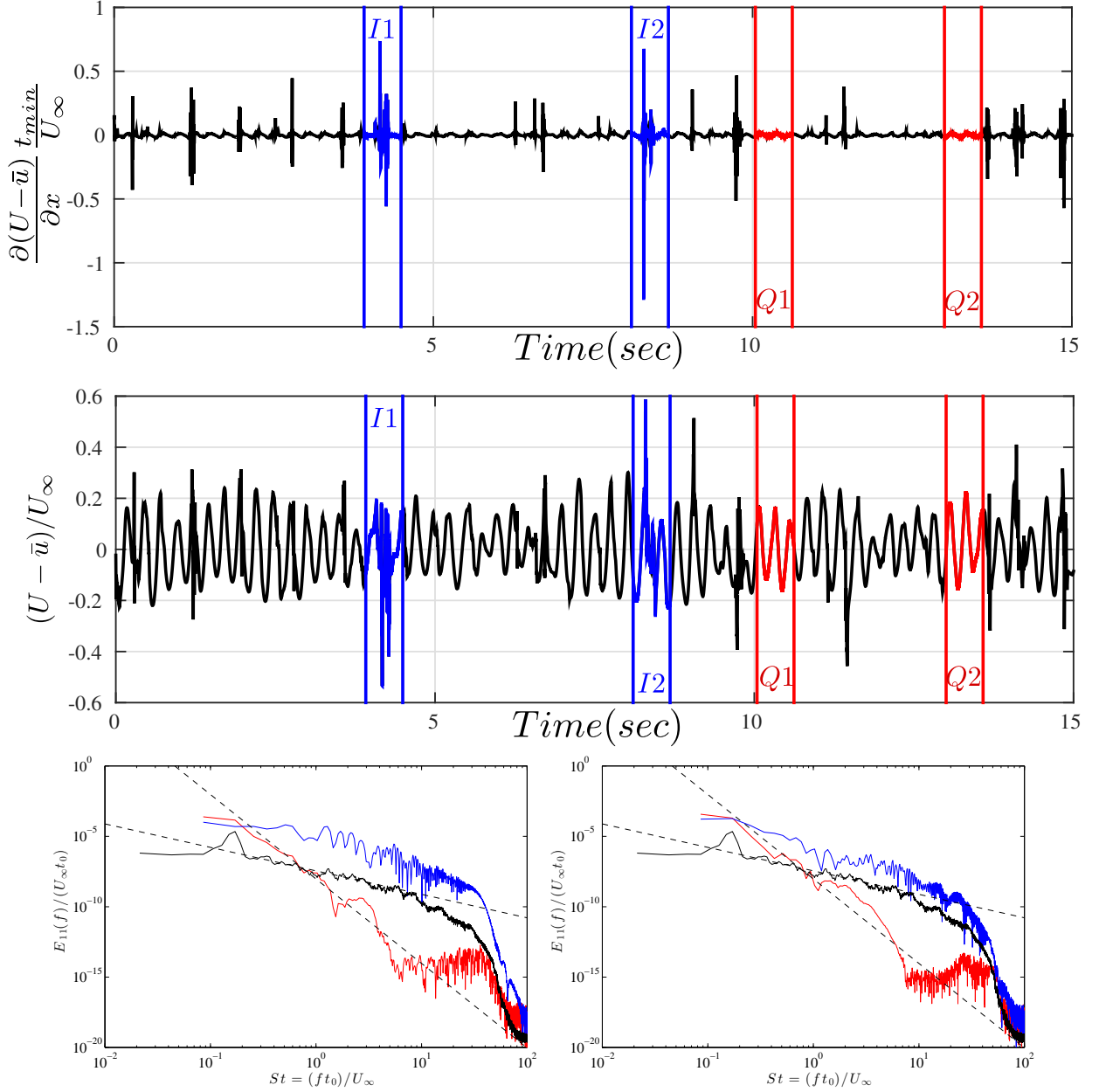
FIG. 9. DNS of turbulent flow generated by SSG (see table 1 and figure 1). (Top) Normalised derivative with respect to the streamwise coordinate of the fluctuating streamwise velocity component $\frac{\partial(U-\overline{u})}{\partial x}\frac{t_{min}}{U_\infty}$ (where $\overline{u}$ is the time-average of U and u' is the rms of $U - \overline{u}$) at $x = 0.3x_*$ as a function of time in seconds ($t_0/U_\infty \approx 0.037s$). (Middle) Normalised fluctuating streamwise velocity component $(U - \overline{u})/U_\infty$ as a function of time in seconds. Intense events I1 and I2 (in blue) and quiescent regions Q1 and Q2 (in red) are identified in the plot. (Bottom) Log-log plots of normalised spectra $E_{11}(f)/(U_\infty t_0)$ versus $St = ft_0/U_\infty$ for the entire signal (in black) and for (left) I1 and Q1 and (right) I2 and Q2. The dash lines correspond to $St^{-5/3}$ and to St^{-6}. The spectra of I1 and I2 (in blue) have much more energy than the spectra of Q1 and Q2 (in red).
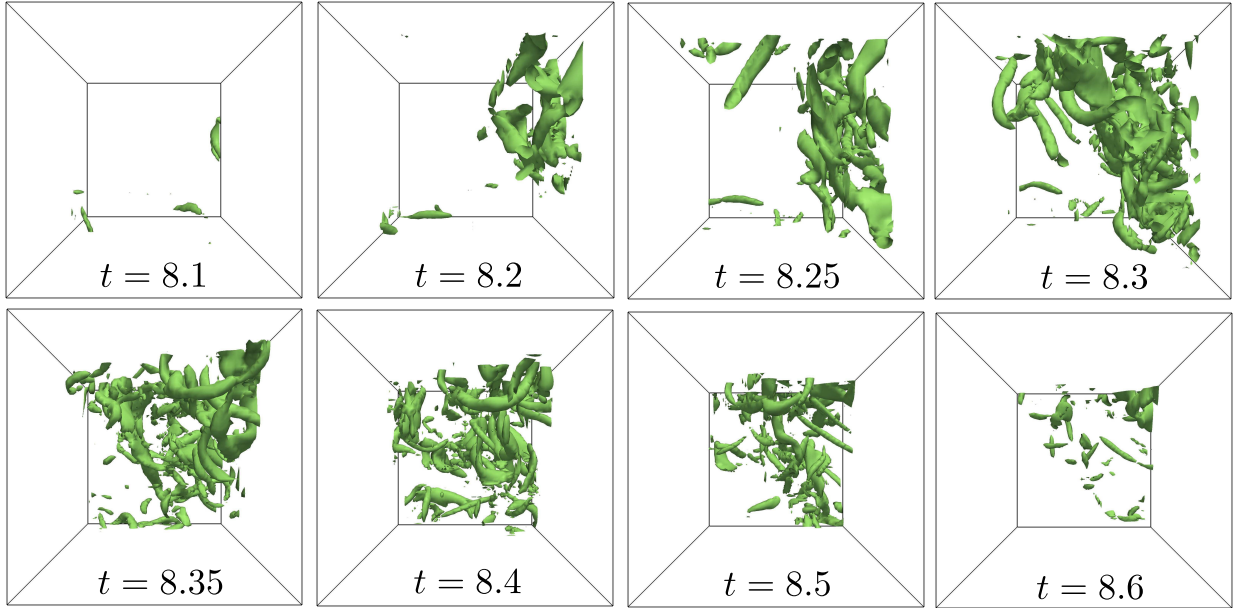
17

FIG. 10. DNS of turbulent flow generated by SSG (see table 1 and figure 1). Visualisations of the enstrophy iso-contours equal to $0.6(U_\infty/t_0)^2$, corresponding to 60% of the maximum value of the entrophy in the cube over the time considered. The visualised 3D box is centred at $x = 0.3x_*$, $y = 0$, $z = 0$, which is the position where figure 9 was recorded, and extends by $\pm 0.125L_0$ in the x directions and by $\pm 0.075L_0$ in the other two directions. There are eight visualised 3D boxes each one corresponding to a different time within the time frame of I2 in figure 9.

data. The $-5/3$ power-law frequency spectrum results from clusters of elongated vortices interwoven with each other and the intermittency of their appearance.

Power-law energy spectra with $-5/3$ power-law exponents are predicted by Kolmogorov phenomenology (see[32]) for wavenumber spectra, not frequency spectra. Frequency spectra with $-5/3$ power-law shapes are usually derived from Kolmogorov wavenumber spectra either when the Taylor frozen turbulence hypothesis can be invoked (see[38]) or when random advection of inertial-scale eddies by large-scale motions is fast enough,[39]. In the Appendix we briefly investigate the Taylor frozen turbulence hypothesis in our DNS flows and find that in the streamwise locations where the data for this paper's figures have been recorded the Taylor frozen turbulence hypothesis can only be approximately applied at frequencies ft_0/U_∞ larger than about 1 or 2. The frequency U_∞/t_0 falls about the centre of the frequency range where the $f^{-5/3}$ spectrum is observed (see figure 5).

The position x_{53} is one where the turbulence is very non-Gaussian and characterised

by intermittent appearances of clusters of intense entangled vortex tubes. It is hard to imagine such vortex tube tangles being dynamically passive. One should therefore not expect the $-5/3$ frequency spectra to translate into $-5/3$ wavenumber spectra in the production region, not only because of the dynamic nature of the vortex tangle but also because of the inhomogeneity of the flow in that region. Further downstream beyond x_{peak} where the turbulence is more homogeneous (see[13,26]) and where the Taylor frozen turbulence hypothesis holds, $k^{-5/3}$ energy wavenumber spectra have been observed in turbulent flows such as the ones studied here ([16,26]). The question which therefore now arises is whether these $-5/3$ wavenumber spectra in the approximately homogeneous and Gaussian decay region originate from the $-5/3$ frequency spectra in the inhomogeneous and non-Gaussian production region. Also, now that we know that the $-5/3$ frequency spectra in the inhomogeneous and non-Gaussian production region result from the intense vortex clusters which are present there intermittently, an equally important question to understand exactly how.

Appendix A: Taylor's frozen turbulence hypothesis

The Taylor frozen turbulence hypothesis permits a direct linear relation between wavenumber and frequency spectra. Since its introduction by[40] nearly eighty years ago its validity has been a constant research theme in the turbulence community with important contributions made, for example, by[41] and[38] (see also[42]). Spatial inhomogeneities and anisotropies have been identified as significant factors limiting the validity of Taylor's hypothesis. More recently, the advent of Direct Numerical Simulations (DNS) has provided the opportunity to use spatio-temporal DNS data to assess this hypothesis. A number of such DNS studies

have already been published with significant results, see for example[43] for spatially evolving isotropic turbulence,[44] for turbulent channel flow and[45] for grid turbulence.

The DNS study of[45] reports good agreement between spatially and temporally averaged statistics beyond a relatively short distance downstream of the grid. Their grid is different from ours and from grids used in actual wind tunnel experiments. Also, the distance where they find that these two types of averages coincide is further downstream from the distances of interest in the present paper.

In this Appendix we use the DNS described in section 3 to calculate two-point two-time correlation functions downstream of grids FSG8 and SSG along the centreline region $0.1x_* \leq x \leq x_*$. This region includes parts of the production region $0 < x < x_{peak}$, the peak of turbulence intensity and the near field decay region $x_{peak} < x < x_*$. The use of such correlations to assess Taylor's hypothesis has already been made by[46] and[43] amongst others.

The actual two-point two-time correlation function that we calculate is

$$C(x, \delta x, \delta t) \equiv \frac{\langle u(x,t)u(x+\delta x, t+\delta t)\rangle}{\sqrt{\langle u(x,t)^2\rangle \langle u(x+\delta x, t+\delta t)^2\rangle}}$$

where u is the streamwise fluctuating velocity component and the averages are taken over time t. An example of this correlation is plotted as a function of normalised time difference $\delta t U_\infty/t_0$ in figure 11 (left). This correlation function is taken at $x = 0.3x_*$ on the centreline downstream of SSG and is plotted for five different streamwise separations $\delta x = 0.235t_0, 0.470t_0, 0.94t_0, 1.88t_0$ and $3.76t_0$. Note that $x = 0.3x_*$ is the streamwise centreline distance from the SSG grid with the best defined $-5/3$ frequency spectrum and that it is also the closest distance from the grid with a $-5/3$ spectrum.

Given a spatial separation δx, the position of the maximum of $\frac{\langle u(x,t)u(x+\delta x, t+\delta t)\rangle}{\sqrt{\langle u(x,t)^2\rangle \langle u(x+\delta x, t+\delta t)^2\rangle}}$ gives the time lag $\delta t = \delta t_{max}(x, \delta x)$ for which the correlation is maximum. The right plot in figure 11 shows that this time lag is approximately equal to $\delta x/\bar{u}$ where $\bar{u}(x)$ is the streamwise mean flow velocity at $x = 0.3x_*$. This approximation is good for $\delta t U_\infty/t_0 < 1$. For larger time lags, δt_{max} is smaller than $\delta x/\bar{u}$ but remains an increasing function of $\delta x/\bar{u}$.

In figure 12 we plot iso-contours of the maximum correlation $C(x, \delta x, \delta t_{max}(x, \delta x))$ as functions of x/x_* and $\delta x/t_0$. Our results show that $C(x, \delta x, \delta t_{max}(x, \delta x))$ is larger than 0.9 at all values of x/x_* for $\delta x/t_0 < 0.4$ in the SSG case and for $\delta x/t_0 < 1$ in the FSG8 case. Two conclusions can clearly be made from these results. Firstly, in the streamwise locations where the data for this paper's figures have been recorded, the Taylor frozen turbulence
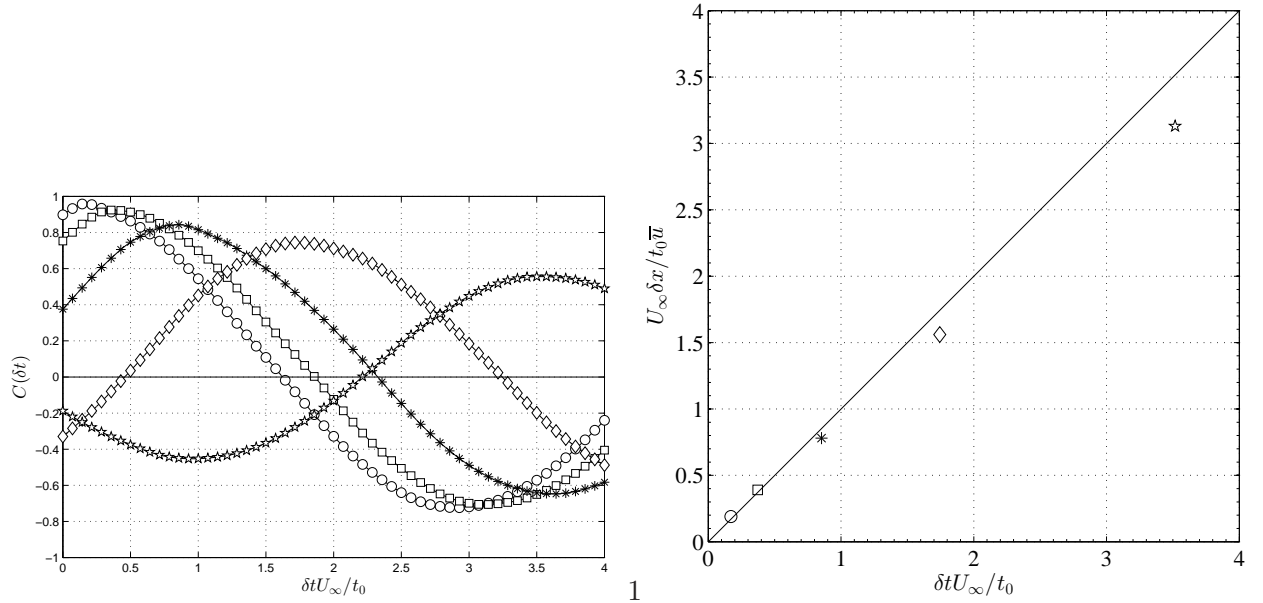
FIG. 11. (Left): The correlation function $C(x, \delta x, \delta t) = \frac{\langle u(x,t)u(x+\delta x, t+\delta t)\rangle}{\sqrt{\langle u(x,t)^2\rangle\langle u(x+\delta x, t+\delta t)^2\rangle}}$ for five different $\delta x = 0.235t_0, 0.470t_0, 0.94t_0, 1.88t_0$ and $3.76t_0$ and $x = 0.3x_*$ on the centreline downstream of SSG. (Right): Relation between $\delta x/\overline{u}$ and δt at the maxima of $C(x, \delta x, \delta t)$ at the same location $x = 0.3x_*$ ($\overline{u}$ is the local mean streamwise velocity).

hypothesis can only be approximately applied at frequencies ft_0/U_∞ larger than about 1 or 2. And secondly, the Taylor frozen turbulence hypothesis is much better obeyed in the very near field of FSG8 than in the very near field of SSG.

REFERENCES

[1] A. Kolmogorov, "Dissipation of energy in locally isotropic turbulence," Dolk. Akad. Nauk SSSR **32**, 19 (1941).

[2] A. Kolmogorov, "The local structure of turbulence in incompressible viscous fluid for very large reynolds numbers," Dolk. Akad. Nauk SSSR **30**, 299 (1941).

[3] A. Townsend, "On the fine-scale structure of turbulence," Proceedings of the Royal Society of London. Series A. Mathematical and Physical Sciences **208**, 534 (1951).

[4] R. Betchov, "An inequality concerning the production of vorticity in isotropic turbulence," J. Fluid Mech. **1(05)**, 497 (1956).

[5] S. Corrsin, "Turbulent dissipation fluctuations," Phys. Fluids **5(10)**, 1301 (1962).
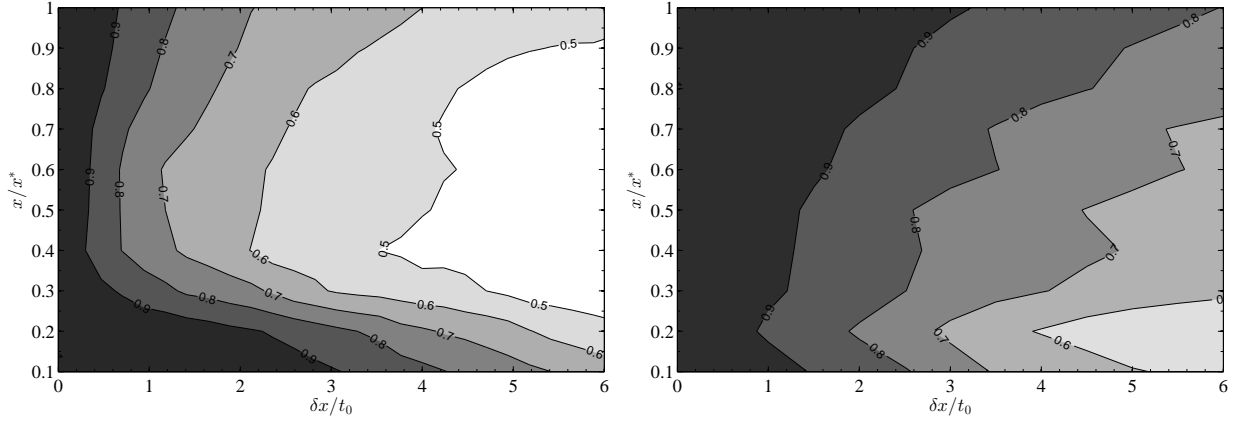
FIG. 12. Estimation of the validity of Taylor's frozen turbulence hypothesis via iso-contours of $C(x, \delta x, \delta t_{max}(x, \delta x))$ plotted here as functions of x/x_* and $\delta x/t_0$. (Left) SSG, (right) FSG8 (see figure 1 and table 1 for details on SSG and FSG8).

[6]H. Tennekes, "Simple model for the small-scale structure of turbulence," Phys. Fluids **11(3)**, 669 (1968).

[7]P. Saffman, "Lectures on homogeneous turbulence," Topics in nonlinear physics pp. 485–614 (1968).

[8]T. Lundgren, "Strained spiral vortex model for turbulent fine structure," Phys. Fluids **25(12)**, 2193 (1982).

[9]A. Gilbert, "A cascade interpretation of lundgren's streched spiral vortex model for turbulent fine structure," Phys. Fluids **5**, 2831 (1993).

[10]S. Saddoughi and S. Veeravalli, "Local isotropy in turbulent boundary layers at high reynolds number," J. Fluid Mech. **268**, 333 (1994).

[11]L. Simmons and C. Salter, "Experimental investigation and analysis of the velocity variations in turbulent flow," Proceedings of the Royal Society of London. Series A. Mathematical and Physical Sciences **145**, 212 (1934).

[12]Jayesh and Z. Warhaft, "Probability distribution, conditional dissipation, and transport of passive temperature fluctuations in grid-generated turbulence," Phys. Fluids **4(10)**, 2292 (1992).

[13]D. Hurst and J. C. Vassilicos, "Scalings and decay of fractal-generated turbulence," Phys. Fluids **19**, 035103 (2007).

[14]P. Krogstad and P. Davidson, "Near-field investigation of turbulence produced by multi-

scale grids," Phys. Fluids **24(3)**, 035103 (2012).

[15] J. Vassilicos, "Dissipation in turbulent flows," Ann. Rev. Fluid Mech. **47**, 95 (2015).

[16] P. Valente and J. C. Vassilicos, "Universal dissipation scaling for non-equilibrium turbulence," Phys. Rev. Lett. **108**, 214503 (2012).

[17] R. Hearst and P. Lavoie, "Decay of turbulence generated by a square-fractal-element grid," J. Fluid Mech. **741**, 567 (2014).

[18] J. Isaza, R. Salazar, and Z. Warhaft, "On grid-generated turbulence in the near-and far field regions," J. Fluid Mech. **753**, 402 (2014).

[19] L. Onsager, "Statistical hydrodynamics," Il Nuovo Cimento (1943-1954) **6**, 279 (1949).

[20] J. Hunt and J. Vassilicos, "Kolmogorov's contributions to the physical and geometrical understanding of small-scale turbulence and recent developments," Proceedings of the Royal Society of London. Series A: Mathematical and Physical Sciences **434(1890)**, 183 (1991).

[21] S. Laizet, J. Vassilicos, and C. Cambon, "Interscale energy transfer in decaying turbulence and vorticity–strain-rate dynamics in grid-generated turbulence," Fluid Dynamics Research **45(6)**, 061408 (2013).

[22] S. Laizet, J. Nedić, and J. Vassilicos, "Influence of the spatial resolution on fine-scale features in dns of turbulence generated by a single square grid," Int. J. of Comp. Fluid Dynamics **in press**, DOI: 10.1080/10618562.2015.1058371 (2015).

[23] R. Gomes-Fernandes, B. Ganapathisubramani, and J. Vassilicos, "Evolution of the velocity-gradient tensor in spatially developing turbulent flow," J. Fluid Mech. **752**, 252 (2014).

[24] Y. Zhou, K. Nagata, Y. Sakai, H. Suzuki, Y. Ito, O. Terashima, and T. Hayase, "Development of turbulence behind the single square grid," Phys. Fluids **26(4)**, 045102 (2014).

[25] Y. Zhou, K. Nagata, Y. Sakai, H. Suzuki, Y. Ito, O. Terashima, and T. Hayase, "Relevance of turbulence behind the single square grid to turbulence generated by regular-and multiscale-grids," Phys. Fluids **26(7)**, 075105 (2014).

[26] N. Mazellier and J. C. Vassilicos, "Turbulence without Richardson-Kolmogorov cascade," Phys. Fluids **22**, 075101 (2010).

[27] S. K. Lele, "Compact finite difference schemes with spectral-like resolution," J. Comp. Phys. **103**, 16 (1992).

[28] S. Laizet and E. Lamballais, "High-order compact schemes for incompressible flows: a

simple and efficient method with the quasi-spectral accuracy," J. Comp. Phys. **228(16)**, 5989 (2009).

[29]S. Laizet and J. C. Vassilicos, "DNS of fractal-generated turbulence," Flow, Turbulence and Combustion **87(4)**, 673 (2011).

[30]S. Laizet and N. Li, "Incompact3d, a powerful tool to tackle turbulence problems with up to $O(10^5)$ computational cores," Int. J. Numer. Methods Fluids **67(11)**, 1735 (2011).

[31]G. I. Taylor, "Statistical theory of turbulence," Royal Soc. London proc. **151 A.**, 421 (1935).

[32]S. Pope, *Turbulent flows* (Cambridge university press, 2000).

[33]D. Sumner, J. Heseltine, and O. Dansereau, "Wake structure of a finite circular cylinder of small aspect ratio," Exp. Fluids **37(5)**, 720 (2004).

[34]M. Braza, R. Perrin, and Y. Hoarau, "Turbulence properties in the cylinder wake at high reynolds numbers," J. of Fluids and Structures **22(6)**, 757 (2006).

[35]Y. Cuypers, A. Maurel, and P. Petitjeans, "Vortex burst as a source of turbulence," Phys. Rev. Lett. **91(19)**, 194502 (2003).

[36]Y. Cuypers, A. Maurel, and P. Petitjeans, "Characterization of an experimental turbulent vortex in the physical and spectral spaces," J. Turbulence **7**, 1 (2006).

[37]C. Cichowlas, P. Bonaiti, F. Debbasch, and M. Brachet, "Effective dissipation and turbulence in spectrally truncated euler flows," Phys. Rev. Lett. **95**, 264502 (2005).

[38]J. Lumley, "Interpretation of time-spectra measured in high-intensity shear flows," Phys. Fluids **8**, 1056 (1965).

[39]H. Tennekes, "Eulerian and lagrangian time microscales in isotropic turbulence," J. Fluid Mech. **67**, 561 (1975).

[40]G. Taylor, "The spectrum of turbulence," Proceedings of the Royal Society of London. Series A-Mathematical and Physical Sciences **164**, 476 (1938).

[41]C. Lin, "On Taylor's hypothesis and the acceleration terms in the navier-stokes equations," J. Applied Math. **10(4)**, 154 (1953).

[42]W. George, H. Hussein, and S. Woodward, in *10th Australasian Fluid Mechanics Conference, volume 2* (Harvard University Press, Melbourne, 1989), pp. 11–15.

[43]S. Lee, S. Lele, and P. Moin, "Simulation of spatially evolving turbulence and the applicability of Taylors hypothesis in compressible flow," Phys. Fluids **4(7)**, 1521 (1992).

[44]J. del Alamo and J. J. Jiménez, "Estimation of turbulent convection velocities and correc-

tions to Taylor's approximation," J. Fluid Mech. **640**, 5 (2009).

[45]L. Djenidi, S. Tardu, and R. Antonia, "Relationship between temporal and spatial averages in grid turbulence," J. Fluid Mech. **730**, 593 (2013).

[46]A. Cenedese, G. Romano, and F. D. Felice, "Experimental testing of Taylor's hypothesis by lda in highly turbulent flow," Exp. Fluids **11(6)**, 351 (1991).